Understanding and Tuning the Electronic Properties of Prussian Blue Analogues

Liangbo Liang[+*], Donald A. Robinson[‡*], Nova Wu[‡], Michael E. Foster[‡], Petro Maksymovych[+], A. Alec Talin[‡], Bobby G. Sumpter[+]

[+]*Center for Nanophase Materials Sciences, Oak Ridge National Laboratory, Oak Ridge, Tennessee 37831, United States*

[‡]*Sandia National Laboratories, Livermore, CA 94550, United States*

[*]Corresponding authors: liangl1@ornl.gov; darobin@sandia.gov.

Abstract: Prussian blue analogs (PBAs) have attracted increasing interest owing to their potential application in various fields such as energy storage and conversion, neuromorphic computing, magnetic switching, etc. With a general formula of $A_xM_N[M_C(CN)_6]$, they feature an open framework that provides abundant channels for diffusion of alkali metal ions A, and allows flexible compositional control of transition metal ions M_N and M_C. The oxidation states of transition metal ions can be tuned by adjusting the amount (x) of alkali ions A. Here we carried out density functional theory calculations combined with experimental measurements to investigate the effects of transition metal ions, alkali ions, and oxidation states on the electronic properties of PBAs. Our calculations found that the band gaps of PBAs can be tuned from close to 0 eV to more than 4 eV. Experimentally, we introduced the synthesis/characterization of five previously unreported PBAs (M_N = Ru, Os, M_C = Fe, Ru, Os) to complete the nine stable M_N:M_C transition metal combinations in group VIII of the periodic table. The optically measured intervalence charge transfer excitation energies of group VIII PBAs are consistent with calculated band gaps. They demonstrate wide band gap tunability by adjusting transition metals and oxidation states, enabling semiconductor-to-metal transitions for memristor applications, and enhancing electronic conductivity for battery applications. This work provides a computational/experimental database of electronic properties versus structural compositions for PBAs.

Keywords: Prussian blue analogs; density functional theory; transition metals; electronic band gap; electronic conductivity; intervalence charge transfer; coordination frameworks

---

Introduction

Prussian blue analogs (PBAs) are inorganic framework materials that have been extensively explored because of their technological potential in diverse fields such as battery electrodes for energy storage/conversion,[1,2,3,4,5,6,7] chemical and bio-sensors,[8,9] artificial synapses for neuromorphic computing,[10] magnetic switching for spintronics,[11,12,13] catalysis for oxygen evolution and water splitting,[14,15,16] etc. These metal hexacyanometallates have a general chemical formula of $A_xM_N[M_C(CN)_6]$, where A is an alkali (Li^+, Na^+, K^+, Rb^+, or Cs^+) and alkaline earth (Mg^{2+}, Ca^{2+}, Sr^{2+}, or Ba^{2+}) ions, M_N and M_C are transition metals ions respectively coordinated to nitrogen and carbon atoms as differentiated by the subscripts, and x indicates the amount of ions intercalated in the open framework of PBAs (see **Figure 1**).[17,18,19,20,21,22] PBAs feature a stable, open framework that provides abundant channels for diffusion and storage of various charge-carrier ions A, and allows flexible compositional control of transition metal ions M_N and M_C (M_N or M_C = Fe, Mn, Co, Cu, Ni, Ru, Os, etc.).[17,18,19,20,21,22] The oxidation states of two transition-metal centers can be tuned by adjusting x (x = 0, 1, 2), and their magnetic configurations can also be manipulated by transition metal selection and x.[17] The high degree of chemical and electrochemical tunability, combined with stability and general non-toxicity, are the main motivators for diverse applications of PBAs.

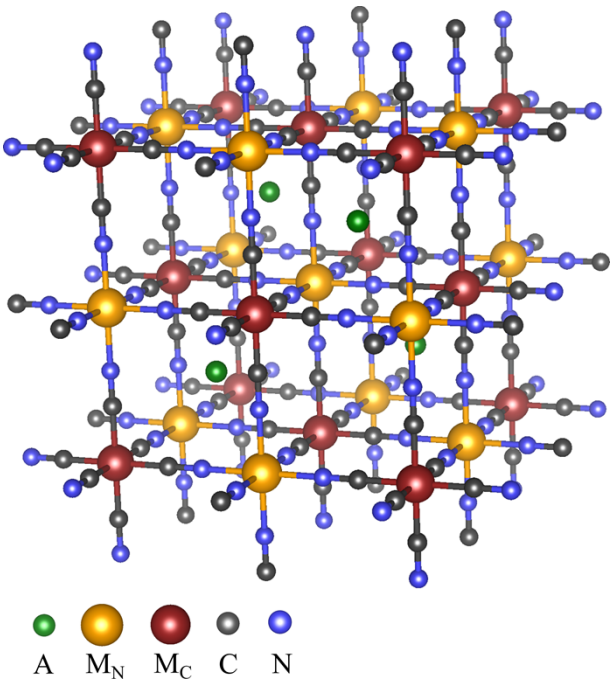

Figure 1. Crystal structure of PBA with a general formula of $A_xM_N[M_C(CN)_6]$, where A is often an alkali metal, M_N and M_C are transition metals octahedrally coordinated to nitrogen and carbon atoms, respectively. PBA structures feature a cubic geometry with wide open space for storage and conduction of alkali metal ions.

The structural versatility in PBAs, however, renders the understanding of structure-property relationships challenging. Experimental works are often limited to few PBA systems. Even though different experimental works studied PBAs with different transition metal ions, alkali ions, and/or oxidation states, their findings cannot be directly compared due to varied experimental conditions. First-principles density functional theory (DFT) calculations can potentially address this problem by systematically simulating PBAs with a wide range of structural parameters under the same calculation condition. However, this approach is hindered by the difficulty of using DFT to describe the strongly correlated *d* orbital electrons and the frequent underestimation of the electronic band gaps.[17,23,24] The strong correlation can be accounted for by adding a Hubbard *U* term in DFT without substantially increasing the computational cost.[19] The DFT+*U* method is a common approach for the band gap correction for systems with *d* and *f* orbitals. Nevertheless, the *U* parameter has to be carefully selected in order to match the calculated band gaps to values from experiments or from more accurate computation methods.[17] For hypothetical PBAs without experimental data, the DFT+*U* method becomes unreliable. Furthermore, PBAs with different transition metal ions need different *U* parameters. Finally, PBAs have two non-equivalent transition metal sites that require two different *U* values for a single PBA structure (even in the case that the two sites are occupied by the same transition metal element),[23,25] which further complicates the problem. Clearly, a more advanced *ab initio* method is highly desirable. Hybrid functionals have been shown to improve DFT results notably by mixing a certain amount of exact exchange from the Hartree-Fock theory into the Kohn-Sham functional,[26] albeit with substantially increased computational cost. They have been successfully applied to PBAs.[10, 17, 18,22,23] Among various hybrid functionals, the nonlocal hybrid Heyd-Scuseria-Ernzerhof (HSE06) functional has been widely used for band gap predictions of PBAs.[10,17,18] However, the number of PBA structures studied by prior hybrid functional DFT works is limited. In the best-case scenario, Hurlbutt et al.[17] theoretically investigated three transition metal elements (Fe, Mn, Co), while most of other works[18,21,22] explored only one or two transition metal elements. A systematic investigation of PBAs with a variety of transition metal ions under the same calculation condition is still lacking.

In this work, we considered a wide range of transition metal ions (Fe, Mn, Co, Cu, Ni, Ru, Os) for both nitrogen-coordinated and carbon-coordinated metal sites (i.e., M_N and M_C), and used the same hybrid HSE06 functional and other parameters in DFT calculations (see Method section) to generate a computational library of electronic properties of PBAs. The consistency in our calculations ensures that we can directly compare band gaps between PBAs with different M_N and M_C ions. As a result, it was found out that the band gaps of PBAs can be tuned from almost 0 eV to more than 4 eV. Interestingly, PBAs with transition metal ions of Ru and Os, the same family member of Fe (i.e., group VIII metals), demonstrate wide tunability of the band gap ranging between 0.17 eV and 2.12 eV when

the alkali ion is potassium. The calculated band gaps of group VIII transition metal PBAs are corroborated by the experimental optical spectroscopic measurements. In addition to the electronic band gaps, the ground state magnetic configurations and magnetic moments were also found to vary strongly by changing the transition metal ions. For group VIII transition metal PBAs, the effects of alkali ions and oxidation states on the electronic and magnetic properties of PBAs were also explored. While changing potassium (K) to lithium (Li) has little effect on the band gap and magnetic configuration of PBAs, changing oxidation states of M_N and M_C by tuning the amount of alkali ions intercalated in PBAs can strongly affect their electronic and magnetic properties, inducing transitions from insulator to semiconductor to (quasi)metal. Our findings revealed how transition metal ions and their oxidation states govern the properties of PBAs, which can be utilized to optimize the electronic conductivities of PBAs-based battery electrodes and to enable semiconductor-to-metal transitions for memristor and neuromorphic computing applications.

Results and Discussion

Effects of transition metal ions on PBAs. PBAs with a single potassium atom in the primitive unit cell, i.e., $KM_N[M_C(CN)_6]$, are in a mixed-valence state. When both transition metal centers M_N and M_C are occupied by Fe atoms, the formula becomes the well-known $KFe[Fe(CN)_6]$, corresponding to the original Prussian blue (PB) compound that has been extensively studied. In its ground state, the nitrogen-coordinated Fe ion (Fe^{3+}) is in a high-spin (hs) electronic configuration, while the carbon-coordinated Fe ion (Fe^{2+}) assumes a low-spin (ls) electronic configuration.[17,18,23] Its band gap is estimated at 1.75 eV, according to optical absorption.[27] When one or two metal centers (M_N or/and M_C) are substituted by other transition metal elements, the electronic and magnetic properties are substantially affected. In general, M_N can be in a hs or ls magnetic configuration, while M_C assumes a ls configuration, leading to either (hs, ls) or (ls, ls) configuration. We simulated both configurations in our DFT-HSE06 calculations to determine which one is energetically more stable. According to a prior theoretical work,[17] the HSE06 method is more accurate for the magnetic ground state compared to the conventional semi-local functionals like the generalized-gradient-approximation Perdew-Burke-Ernzerhof (PBE) functional. We considered 6 other transition metal ions (Mn, Co, Cu, Ni, Ru, Os) besides Fe for both M_N and M_C sites, giving rise to 18 PBA compounds besides $KFe[Fe(CN)_6]$, as shown in **Table 1**. Although Hurlbutt et al.[17] studied three metal elements (Fe, Mn, Co), the substitution was limited to the M_N site while M_C remained fixed as Fe. Here, however, the substitution occurs to both metal centers by more diverse transition metal elements.

Table 1. Band gaps and magnetic moments per formula unit for PBAs with different transition metal ions calculated using the HSE06 functional. (hs, ls) and (ls, ls) indicate different magnetic configurations of two transition metal sites: (high-spin, low-spin) and (low-spin, low-spin).

	Band gap (eV)	Magnetic moment (μ_B)		Band gap (eV)	Magnetic moment (μ_B)
$KFe[Fe(CN)_6]$	2.12	5.0 (hs, ls)			
$KFe[Mn(CN)_6]$	1.87	2.0 (ls, ls)	$KFe[Ni(CN)_6]$	1.36	7.0 (hs, ls)
$KMn[Fe(CN)_6]$	2.40	4.0 (hs, ls)	$KNi[Fe(CN)_6]$	2.91	3.0 (ls, ls)
$KMn[Mn(CN)_6]$	1.17	5.0 (hs, ls)	$KNi[Ni(CN)_6]$	2.97	3.0 (ls, ls)
$KFe[Co(CN)_6]$	3.00	4.0 (hs, ls)	$KFe[Ru(CN)_6]$	2.07	5.0 (hs, ls)
$KCo[Fe(CN)_6]$	3.59	0.0 (ls, ls)	$KRu[Fe(CN)_6]$	1.06	1.0 (ls, ls)
$KCo[Co(CN)_6]$	4.06	3.0 (hs, ls)	$KRu[Ru(CN)_6]$	0.80	1.0 (ls, ls)
$KFe[Cu(CN)_6]$	1.23	6.0 (hs, ls)	$KFe[Os(CN)_6]$	1.85	5.0 (hs, ls)
$KCu[Fe(CN)_6]$	2.91	0.0 (ls, ls)	$KOs[Fe(CN)_6]$	0.86	1.0 (ls, ls)
$KCu[Cu(CN)_6]$	2.90	1.0 (ls, ls)	$KOs[Os(CN)_6]$	0.17	1.0 (ls, ls)

For the PB compound, $KFe[Fe(CN)_6]$, our HSE06 calculations confirmed that Fe_N and Fe_C assume the (hs, ls) magnetic ground state, consistent with prior works.[17,18,23] The calculated electronic band gap is 2.12 eV (**Table 1**), slightly above the experimental lower bound estimate of ~1.75 eV.[27] Previous calculations using HSE06 predicted the band gap to range from 1.90 eV to 2.31 eV,[10,17,18] corroborating our results. It is important to note that structural distortions (e.g., Jahn-Teller distortion, tetragonal distortion, rhombohedral distortion) to the ideal cubic geometry should be considered in PBAs, which leads to lower symmetry and energy in the materials.[10,17,21,22] To access the more stable lower-symmetry structures, random small perturbations were introduced by us and others to the atomic positions before structural relaxations. We expect that structural distortions introduced in different theoretical works are unavoidably different, which could contribute to the variation of the calculated band gap. Furthermore, the alkali ions vary from Li to Na to K in different works[10,17,18] even though the compound is all called PB, another reason for the band gap variation. Moving on to PBAs with one or two metal centers substituted by other transition metal elements, similar distortions were considered. Hurlbutt et al.[17] studied $NaMn[Fe(CN)_6]$ and $NaCo[Fe(CN)_6]$, and found the band gap to be 2.88 eV and 3.33 eV, respectively. Here, for $KMn[Fe(CN)_6]$ and $KCo[Fe(CN)_6]$, the band gap is 2.40 eV and 3.59 eV, respectively. Considering the effects of different alkali ions and structural distortions, our results are in line with those of the prior work,[17] underscoring the validity

of our predictions. The calculated band gap, magnetic configuration, and magnetic moment per formula unit are found to vary strongly with the choices of M_N and M_C, as shown in **Table 1**. For example, the band gap can be as low as 0.17 eV for $KOs[Os(CN)_6]$ and as high as 4.06 eV for $KCo[Co(CN)_6]$. $KFe[Ni(CN)_6]$ assumes a (hs, ls) configuration with a large magnetic moment of 7.0 μ_B, while $KCo[Fe(CN)_6]$ and $KCu[Fe(CN)_6]$ assume a (ls, ls) configuration with a zero magnetic moment. The results illustrated in **Table 1** serve as a guiding map for targeted experimental synthesis and applications of PBAs.

Most of PBAs studied in **Table 1** have the band gap close to or larger than 2 eV, and some of them have the band gap close to or larger than 3 eV, so they are either large-gap semiconductors or insulators, and therefore do not have considerable populations of thermally generated charge carriers at room temperature. The exceptions are $KMn[Mn(CN)_6]$ with a 1.17 eV gap, $KFe[Cu(CN)_6]$ with a 1.23 eV gap, $KFe[Ni(CN)_6]$ with a 1.36 eV gap, and most of PBAs substituted with Ru and Os. In fact, among all transition metal ions explored, group VIII metal elements Fe, Ru, and Os lead to the largest relative changes of the band gap between 0.17 eV and 2.12 eV. For instance, $KRu[Ru(CN)_6]$ has a band gap of 0.80 eV and $KOs[Os(CN)_6]$ has a band gap of 0.17 eV, compared to $KFe[Fe(CN)_6]$ with a band gap of 2.12 eV. Such dramatic reductions of the band gap enhance the electronic conductivity of the PBAs and lay out the foundation for achieving semiconductor-to-metal transitions in applications of neuromorphic computing, as will be discussed below.

To understand why Ru and Os can strongly affect the electronic properties of PBAs, we computed atom-projected density of states (DOS) and electronic band structures of $KFe[Fe(CN)_6]$, $KFe[Ru(CN)_6]$, $KRu[Fe(CN)_6]$, and $KRu[Ru(CN)_6]$, as shown in **Figure 2** and **Figure 3**, respectively. For $KFe[Fe(CN)_6]$, the valence band edge states originate from spin-down, carbon-coordinated Fe orbitals (i.e., Fe_C, see the red line in **Figure 2a**), but the conduction band edge states almost solely arise from spin-down, nitrogen-coordinated Fe orbitals (i.e., Fe_N, the blue line). According to the band structure in **Figure 3a**, the valence bands and conduction bands near the Fermi level are fairly flat, indicating that the valance band edge states are localized on the Fe_C site while the conduction band edge states are localized on the Fe_N site, consistent with the PDOS analysis.[17] This suggests that the lowest energy excitation requires the electron transfer from one metal center to the other one, in agree with the experimental observation.[27] The flat bands and localized orbitals also indicate heavy effective masses for both electrons and holes in $KFe[Fe(CN)_6]$.[10,17] For $KFe[Ru(CN)_6]$ where the Fe_C site is substituted by Ru to become Ru_C, the Fe_N site still assumes the high-spin configuration and the Ru_C site remains in the low-spin configuration, just like $KFe[Fe(CN)_6]$. Because Ru belongs to the same family as Fe, it does not introduce notable changes to both PDOS (**Figure 2b**) and band structure (**Figure 3b**), compared to those of $KFe[Fe(CN)_6]$. The valence band and conduction band edge states are still dominated by the spin-down orbitals of carbon-coordinated metal site (Ru_C) and nitrogen-

coordinated metal site (Fe_N), respectively. The only difference is that Ru orbitals are less localized due to its larger atomic radius than Fe, and thus the Ru_C center renders the edge bands less flat, leading to a slightly reduced band gap of 2.07 eV for $KFe[Ru(CN)_6]$.

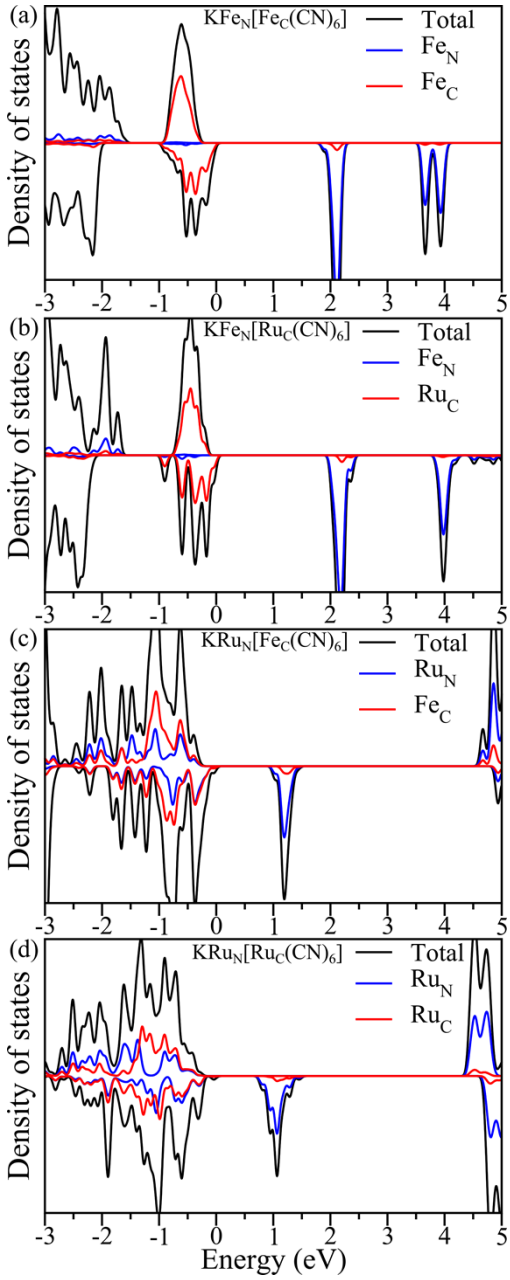

Figure 2. HSE06 calculated total and atom-projected density of states (DOS) of PBAs with group VIII transition metal elements. The Fermi energy is set at 0 eV.

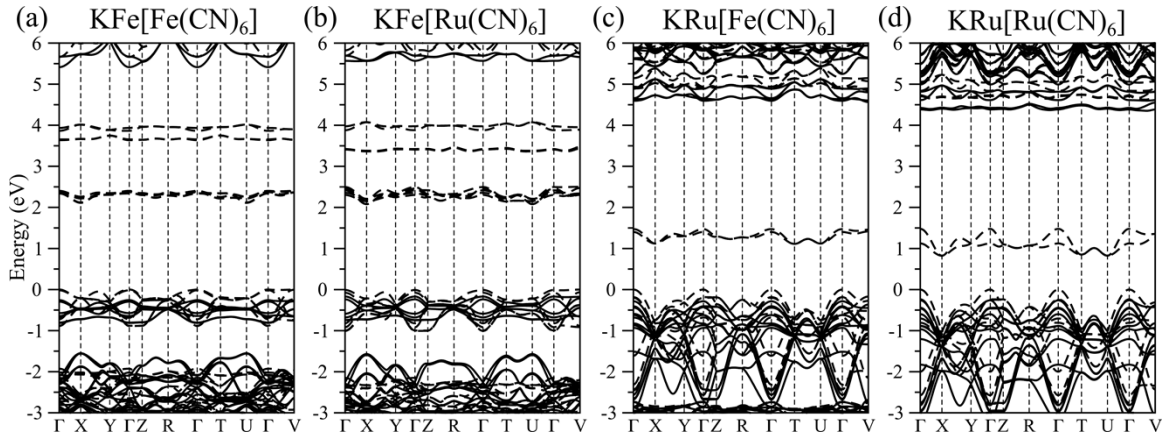

Figure 3. HSE06 calculated electronic band structures of PBAs with group VIII transition metal elements. The Fermi energy is set at 0 eV. Solid and dashed lines correspond to spin up and down channels, respectively. Both valence and conduction band edges arise from the same spin channel.

Moving on to $KRu[Fe(CN)_6]$ where the Fe_N site is substituted by Ru to become Ru_N, the situation is changed drastically. Unlike the previous two compounds in which the Fe_N site prefers the high-spin configuration, our calculations found that the Ru_N site prefers the low-spin configuration, giving rise to the overall (ls, ls) magnetic configuration in $KRu[Fe(CN)_6]$ in contrast to the (hs, ls) configuration in $KFe[Fe(CN)_6]$. With both N-coordinated and C-coordinated metal centers as low spin, there is better energy alignment between neighboring metal sites and a more delocalized electronic structure for $KRu[Fe(CN)_6]$.[10] This can be seen by the significant changes in both PDOS (**Figure 2c**) and band structure (**Figure 3c**). The conduction band edge states still primarily originate from spin-down, nitrogen-coordinated metal orbitals (Ru_N, the blue line). However, the valence band edge states are no longer exclusively from spin-down, carbon-coordinated metal orbitals, but instead from a nearly equal mixture of both Ru_N and Fe_C orbitals (see the overlapping blue and red lines below the Fermi level in **Figure 2c**), indicating that the same low-spin configuration in both metal centers does result in the delocalization and hybridization between the orbitals of the two metal centers. Consequently, the valence bands of $KRu[Fe(CN)_6]$ in **Figure 3c** are much more dispersive. Since the conduction bands near the Fermi level are from the Ru orbitals instead of Fe ones, they are also more dispersive. Therefore, the effective masses for both electrons and holes become smaller. The larger band dispersions combined with the fact that both the valence and conduction band edge states are associated with the orbitals of the Ru_N site, the band gap of $KRu[Fe(CN)_6]$ is significantly reduced by half to 1.06 eV. Similar analysis can be made for $KRu[Ru(CN)_6]$ that also prefers the (ls, ls) magnetic configuration. Its PDOS (**Figure 2d**) and band structure (**Figure 3d**) resemble very much those of $KRu[Fe(CN)_6]$, just like that $KFe[Fe(CN)_6]$ and $KFe[Ru(CN)_6]$ share the same (hs, ls) magnetic configuration and resemble each other. The only difference between $KRu[Fe(CN)_6]$ and $KRu[Ru(CN)_6]$ is

that Ru atoms occupy both metal centers in the latter and thus the bands are more dispersive, leading to a smaller band gap (0.80 eV) and smaller effective masses of electrons and holes.[10] In short, as illustrated in **Figure 3**, from (a) to (d), the bands near the Fermi level become more dispersive and the band gap is continuously decreasing, and therefore the electronic conductivity is increasing, as confirmed by prior experimental measurements that showed two orders of magnitude increase from PB to Ru-PBAs.[10,28]

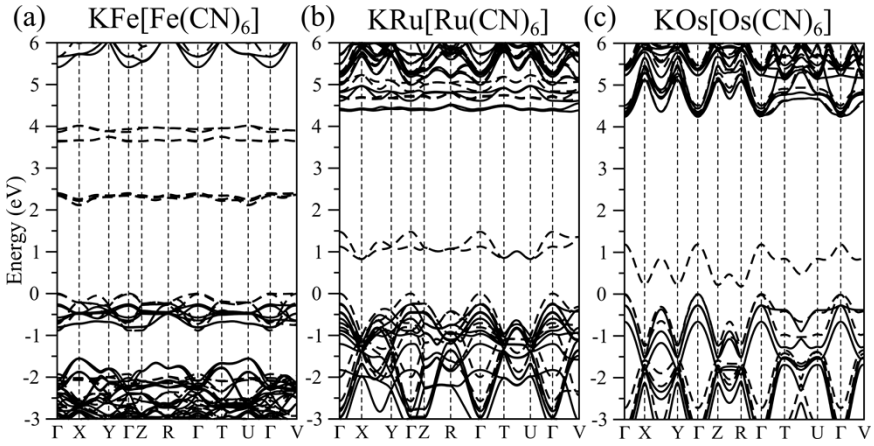

Figure 4. HSE06 calculated electronic band structures of three PBAs composed of group VIII metals. The Fermi energy is set at 0 eV. Solid and dashed lines correspond to spin up and down channels, respectively.

Finally, when it comes to Os-PBAs in **Table 1**, similar analysis can be made following the logic of Ru-PBAs. The larger atomic radius of Os than Ru, however, gives rise to more delocalized orbitals and thus smaller band gaps for Os-PBAs, as illustrated in **Figure 4**. From Fe to Ru to Os, it is evident that the bands near the Fermi level get more dispersive and the band gap decreases. Both $KRu[Ru(CN)_6]$ and $KOs[Os(CN)_6]$ prefer the (ls, ls) magnetic configuration and they share similar electronic band structure. However, the conduction bands of $KOs[Os(CN)_6]$ are notably more dispersive, contributing to its small indirect band gap. In specific, the band gap of $KOs[Os(CN)_6]$ is 0.17 eV while that of $KRu[Ru(CN)_6]$ is 0.80 eV. Our calculations provide strong evidence that Ru and Os can play a key role in engineering of PBAs for targeted functionalities.

UV-Vis-NIR spectroscopy of group VIII PBAs. To evaluate DFT results, nine PBAs based on the group VIII metals (Fe, Ru, Os) were synthesized. To the best of our knowledge, the compounds, $Ru:Fe(CN)_6$, $Os:Fe(CN)_6$, $Os:Ru(CN)_6$, $Ru:Os(CN)_6$, and $Os:Os(CN)_6$ have not previously been reported in the literature. All compounds were synthesized with $K_4M(CN)_6$ salts as starting materials, so are assumed to contain potassium ions to balance charge and adopt a mixed valence state, similar to so-called "soluble" Prussian blue.[29,30] Each compound gives a unique UV-Vis-NIR absorption spectrum (**Figure 5**), with all spectra showing evidence optically excited charge transfer from one metal center to another,

commonly known as intervalence charge transfer (IVCT) transitions.[10, 28] For example, the charge-localized ground state of Prussian blue, Fe^{III}-NC-Fe^{II} (labelled Fe-Fe in **Figure 5a**), undergoes IVCT between Fe_C donors and Fe_N acceptors to form Fe^{II}-NC-Fe^{III} excited states, consistent with our theoretical analysis in **Figure 2a** and **Figure 3a** above.

Figure 5a shows the IVCT spectra for PBAs where iron is a common acceptor (M_N = Fe) and the M_C donor is substituted with Fe, Ru, or Os. The general trend of ν(Fe-Fe) < ν-(Fe-Os) < ν(Fe-Ru) for the IVCT band manifolds is consistent with the previous observations of Robin,[27] who also noted similar shifts for the metal-to-ligand charge transfer (MLCT) peak energies of $M_C(CN)_6^{4-}$, where the CN^- ligand is the common acceptor. However, this ranking of $\nu(M_N\text{-Fe}) < \nu(M_N\text{-Os}) < \nu(M_N\text{-Ru})$ for the IVCT maximum is not observed for the case of the Ru-M_C PBAs, as shown in **Figure 5b**, where the order is ν(Ru-Ru) < ν(Ru-Fe) < ν(Ru-Os). The ranking of IVCT peak energies for the Os-M_C PBAs (**Figure 5c**) is somewhat comparable to that of the Fe-M_C PBAs in **Figure 5a**, where M_N-Ru is the compound with the highest IVCT energy for both sets.

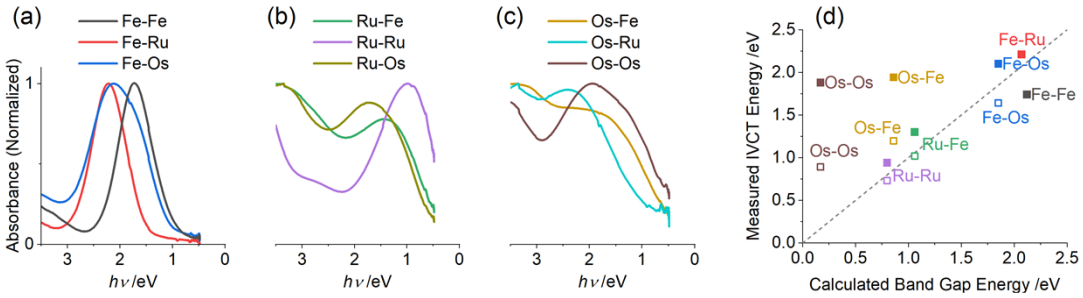

Figure 5. (a-c) Measured UV-Vis-NIR absorption spectra for nine different PBAs composed of group VIII metals, each labelled as M_N-M_C. The IVCT bands for all compounds are below 3 eV. **(d)** Measured IVCT band manifolds plotted versus calculated band gaps of $KM_N[M_C(CN)_6]$ for seven different PBA combinations. Dashed gray line marks a slope of unity. Closed symbols represent the IVCT peak maxima assuming only one IVCT transition. Open symbols represent the IVCT peak maxima of the lowest energy peaks obtained after deconvolution assuming multiple overlapping bands (See Figure S1 of Supporting Information). For Fe-Fe and Fe-Ru, only one band is considered.

Comparison of calculated bandgaps to IVCT excitation energies. **Figure 5d** shows the measured IVCT band manifolds of seven group VIII PBAs plotted versus the calculated band gaps (see **Table 1**). Good agreement is observed for Ru-Ru, Ru-Fe, Fe-Os, Fe-Ru, and Fe-Fe. There is notable discrepancy between measured IVCT band manifolds (closed symbols obtained by assuming only one IVCT transition) and calculated bandgaps of Os-Fe and Os-Os. However, we note that only the Fe-Fe and Fe-Ru IVCT bands can be fitted with a single Gaussian peak, whereas the other spectra require fitting at least two overlapping peaks for deconvolution. We therefore put more confidence in the

measurements of the lowest IVCT energy peaks estimated from deconvolution, open symbols in **Figure 5d**, as an optical descriptor for the bandgap. This treatment provides better theoretical-experimental agreement, but the calculated band gap of the Os-Os PBA is still ~0.7 eV lower than the experimental observation. According to prior works[31,32,33] and our calculations, from Fe to Ru to Os, the correlation effect between electrons becomes weaker. This is reflected in the DFT+*U* calculations where the Hubbard *U* term gets smaller: in general, U^{eff} = 5.5-6.0 for Fe-Fe, U^{eff} = 4.0 for Ru-Ru,[10, 18] while U^{eff} = 2.8-3.4 for Os-Os.[31,32,33] A larger *U* value typically means a larger band gap. The smallest *U* term indicates the smallest band gaps for relatively weakly correlated Os compounds, as confirmed by our DFT+*U* calculations that yield the band gap as 1.81 eV for Fe-Fe, 1.02 eV for Ru-Ru, and 0.32 eV for Os-Os. Our hybrid functional calculations (without the *U* parameter) found similar results as shown in **Table 1**. Therefore, we believe that the inconsistency between the measured IVCT band manifold and calculated bandgap of Os-Os is probably because the band edge absorption peak lies at lower energy than the detection limit (i.e., the Os-Os band gap of 0.17 eV is lower than 0.5 eV cutoff of the spectrometer). Indeed, the tails of the IVCT transitions of Os-M_C PBAs in **Figure 5c** also extend to lower energy mid-infrared regions beyond the limitations of the spectrometer (0.5 eV cutoff). In short, the absorption measurements generally support the DFT predictions on the band gaps of group VIII PBAs.

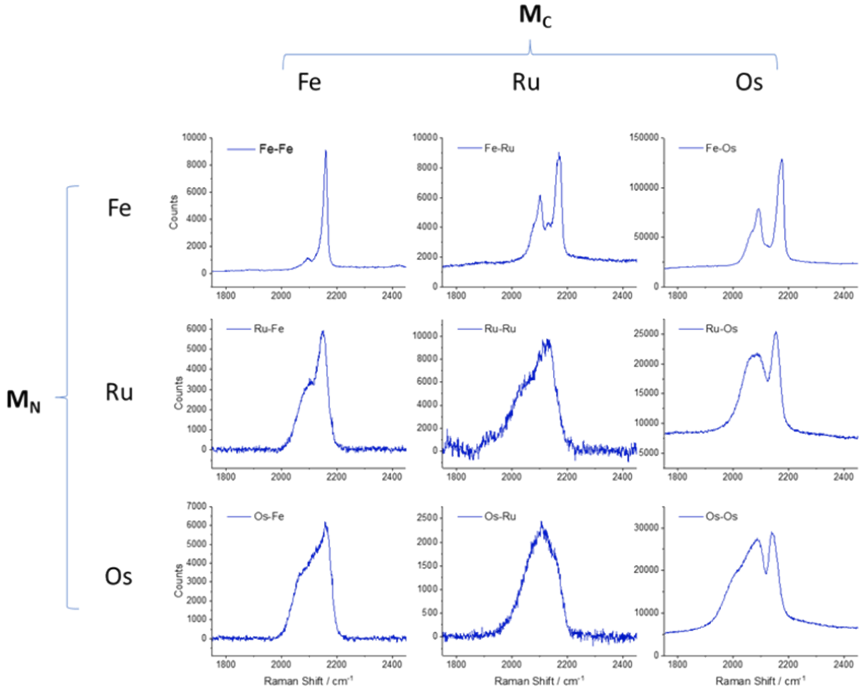

Figure 6. Measured Raman spectra of the C≡N stretch for M_N-M_C PBAs samples.

Raman spectroscopy of cyanide bridging ligand stretch. The measured Raman peaks for the CN stretch vibrations are shown in **Figure 6**. The Fe_N-M_C PBAs exhibit sharper Raman

peaks than the Ru_N-M_C and Os_N-M_C PBAs samples, suggesting that the latter may have the poorer crystallinity, as also shown by X-ray diffraction (Figure S2 in SI). However, it is well documented that broader and more coalesced peak shapes for the CN vibrations occur in mixed-valence CN-bridged trinuclear Ru-Ru-Ru molecular complexes with higher degrees of electronic delocalization.[34,35,36] Given that the calculated gaps and measured IVCT energies are much lower for Ru_N-M_C and Os_N-M_C PBAs, we attribute the broadened spectral features to both poor crystallinity and high metal-metal electronic coupling.

Effects of alkali ions on PBAs. The alkali elements most used in PBAs are lithium (Li), sodium (Na) and potassium (K), leading to lithium-, sodium-, and potassium-ion batteries, respectively. The large empty space in PBAs (**Figure 1**) provides multiple locations for the intercalation of cations. With increasing ionic size, the preferable intercalation location changes from the face-centered to body-centered site.[19] In general, the smaller cations such as Li^+ and Na^+ prefer to occupy the face-centered location, whereas the larger cations such as K^+ are more energetically stable in the body center of the cubic framework. Because the hybrid functional calculations are substantially more computationally costly than conventional DFT and DFT+*U* calculations, it is practically impossible to study all possible intercalated cations for all PBAs (in fact, prior hybrid functional works only studied one type of alkali ion).[10,17,18,23] Therefore, we chose the Li and K, the lower end and upper end in terms of ionic size, to investigate the effects of alkali ions on group VIII transition metal PBAs, as shown in **Table 2**. Among all 7 compounds, changing from K to Li ion does not introduce notable changes in either the band gap, magnetic configuration, or magnetic moment. This is understandable because these properties are mostly determined by the transition metal ions. As discussed above, the valence and conduction band edge states are primarily contributed by M_N and M_C orbitals, and the spins almost exclusively arise from M_N and M_C as well. Therefore, the alkali ions exert negligible influence on the electronic and magnetic properties of PBAs.

Table 2. Band gaps and magnetic moments per formula unit for group VIII metal PBAs with different alkaline cations calculated using the HSE06 functional.

	Band gap (eV)	Magnetic moment (μ_B)		Band gap (eV)	Magnetic moment (μ_B)
$KFe[Fe(CN)_6]$	2.12	5.0	$LiFe[Fe(CN)_6]$	1.93	5.0
$KFe[Ru(CN)_6]$	2.07	5.0	$LiFe[Ru(CN)_6]$	1.88	5.0
$KRu[Fe(CN)_6]$	1.06	1.0	$LiRu[Fe(CN)_6]$	1.11	1.0
$KRu[Ru(CN)_6]$	0.80	1.0	$LiRu[Ru(CN)_6]$	0.84	1.0
$KFe[Os(CN)_6]$	1.85	5.0	$LiFe[Os(CN)_6]$	1.73	5.0
$KOs[Fe(CN)_6]$	0.86	1.0	$LiOs[Fe(CN)_6]$	0.90	1.0

$KOs[Os(CN)_6]$	0.17	1.0	$LiOs[Os(CN)_6]$	0.26	1.0

Table 3. Band gaps and magnetic moments per formula unit for group VIII metal PBAs at different oxidation states and with different alkaline cations calculated using the HSE06 functional. The negative value (-0.17 eV) indicates that $Os[Os(CN)_6]$ is metallic.

	Band gap (eV)	Magnetic moment (μ_B)		Band gap (eV)	Magnetic moment (μ_B)
$Fe[Fe(CN)_6]$	1.89	6.0			
$KFe[Fe(CN)_6]$	2.12	5.0	$LiFe[Fe(CN)_6]$	1.93	5.0
$K_2Fe[Fe(CN)_6]$	3.37	4.0	$Li_2Fe[Fe(CN)_6]$	3.21	4.0
$Ru[Ru(CN)_6]$	0.27	2.0			
$KRu[Ru(CN)_6]$	0.80	1.0	$LiRu[Ru(CN)_6]$	0.84	1.0
$K_2Ru[Ru(CN)_6]$	3.68	0.0	$Li_2Ru[Ru(CN)_6]$	4.22	0.0
$Os[Os(CN)_6]$	-0.17	2.0			
$KOs[Os(CN)_6]$	0.17	1.0	$LiOs[Os(CN)_6]$	0.26	1.0
$K_2Os[Os(CN)_6]$	2.88	0.0	$Li_2Os[Os(CN)_6]$	3.22	0.0

Effects of oxidation states on PBAs. The quantity of alkali metal ions intercalated into the system during redox reactions can substantially affect the electronic properties of the PBAs. In $A_xM_N[M_C(CN)_6]$, x=0 or 2 corresponds to the transition metal oxidation state of III (oxidized) or II (reduced). At x=1, the valency of the transition metals is mixed with a 1:1 ratio of II:III.[17,18] Taking Prussian blue as an example, its oxidation state can be represented as $KFe^{3+}[Fe^{2+}(CN)_6]$; its oxidized form corresponds to $Fe^{3+}[Fe^{3+}(CN)_6]$, called Prussian yellow; the reduced one is $K_2Fe^{2+}[Fe^{2+}(CN)_6]$, called Prussian white.[18, 37] The change of the oxidation states in the two transition metal centers leads to changes in both the band gap and magnetic moment in the unit cell, as shown in **Table 3**. For PB, from $Fe[Fe(CN)_6]$ to $KFe[Fe(CN)_6]$ to $K_2Fe[Fe(CN)_6]$, the band gap varies from 1.89 to 2.12 to 3.37 eV, consistent with the prior theoretical work that considered Na as the alkali ion.[17] Similar results are found by our calculations for the Li ion. Note that the band gaps are all close to or larger than 2 eV. At the reduced form, the band gap is further increased to more than 3 eV, making the system an insulator. The behavior we observed for Ru-Ru and Os-Os PBA compounds is more interesting. Because $KRu[Ru(CN)_6]$ and $KOs[Os(CN)_6]$ have considerably smaller band gaps and much more delocalized orbitals compared to $KFe[Fe(CN)_6]$, their band gap variations with the amount of alkali ions are much more significant. As shown in **Table 3**, from $Ru[Ru(CN)_6]$ to $KRu[Ru(CN)_6]$ to $K_2Ru[Ru(CN)_6]$, the band gap is changed from 0.27 to 0.80 to 3.68 eV, suggesting a quasi-metal to

semiconductor to insulator transition; from $Os[Os(CN)_6]$ to $KOs[Os(CN)_6]$ to $K_2Os[Os(CN)_6]$, the band gap varies from -0.17 to 0.17 to 2.88 eV, demonstrating a metal to insulator transition. Similar results are again found for the Li ion. Our findings indicate that the electrical conductivity of Ru-Ru and Os-Os PBAs can be tuned over a large range via redox reactions utilizing alkali ions for charge balance. This approach is highly useful for designing emerging analog memories for neuromorphic computing and brain computer interfaces.[38] Recently, we demonstrated the application of Ru-Ru PBAs for flexible artificial synapses that reversibly switched conductance by more than four orders of magnitude through electrochemically tuning the amount of Li ions.[10] In addition, Ru-Ru and Os-Os PBAs exhibit higher electronic conductivity than Fe-Fe PB, and thus they are expected to possess great potential in battery cathodes.

Conclusions

In summary, we combined a systematic first-principles DFT investigation of electronic and magnetic properties of PBAs with a variety of transition metal ions (Fe, Mn, Co, Cu, Ni, Ru, Os) using the more accurate hybrid HSE06 functional with UV-Vis-NIR and Raman spectroscopic measurements. We showed that the band gaps of PBAs can be tuned from almost 0 eV to more than 4 eV. The magnetic configurations and magnetic moments also depend on the transition metal ions. We found good agreement between calculated band gaps and optically measured excitation energies for the group VIII PBAs. Interestingly, PBAs containing Ru and Os demonstrate wide tunability of the band gap from 0.17 eV to 2.07 eV. Ru- and Os-PBAs can have significantly smaller band gaps and more dispersive bands near the Fermi level than the original PB, and thus possess enhanced electronic conductivities. For group VIII PBAs, the effects of alkali ions and oxidation states were also studied. While changing potassium (K) to lithium (Li) has negligible effect on the band gap and magnetic configuration of PBAs, changing oxidation states of the transition metal centers by tuning the amount of alkali ions (x) can strongly affect their electronic properties, inducing transitions from (quasi)metal to semiconductor to insulator when x is changed from 0 to 2. Our work clearly demonstrates how transition metal ions and their oxidation states govern the functional properties of PBAs, providing the important guidance on tailoring the electronic conductivities of PBAs-based battery electrodes and showcasing the potential of Ru- and Os-PBAs for memristor and neuromorphic computing applications.

Methods

Materials

Iron(III) trinitrate nonahydrate [$Fe(NO_3)_3 \cdot 9H_2O$], ruthenium(III) trichloride hydrate [$RuCl_3 \cdot xH_2O$], osmium(III) trichloride hydrate [$OsCl_3 \cdot xH_2O$], potassium hexacyanoferrate(II) [$K_4Fe(CN)_6$], potassium hexacyanoruthenate(II) [$K_4Ru(CN)_6$], potassium osmate(VI) dihydrate [$K_2OsO_4 \cdot 2H_2O$], and potassium cyanide [KCN] were procured from Sigma-Aldrich. All water was filtered and deionized to 18.2 MΩ·cm resistivity before use (*PureLab flex* filtration system, ELGA LabWater).

Synthesis of potassium hexacyanoosmate

Potassium hexacyanoosmate, $K_4Os(CN)_6$, was synthesized based on a procedure reported in the literature,[39] but using $K_2OsO_4 \cdot 2H_2O$ in place of K_4OsCl_6 as the osmium precursor. $K_2OsO_4 \cdot 2H_2O$ (1 g) was dissolved in 25 mL of a saturated KCN solution at heated at 80 °C under rapid stirring for 24 hours. The precipitate was collected by centrifugation and rinsed with methanol. The crude $K_4Os(CN)_6$ salt was dissolved in 38 mL water and recrystallized by slow addition of an equal volume of methanol. This recrystallization was carried out twice and the product was rinsed with methanol before drying at room temperature.

Synthesis of group VIII metal hexacyanometallates

Eight of the nine group VIII PBAs were synthesized by a room-temperature coprecipitation method whereby a 10 mL solution containing 50 mM of the metal(III) nitrate or chloride starting material was added drop by drop via syringe to a flask containing 10 mL of 25 mM potassium hexacyanometallate(II) under rapid stirring. Fe:$M'(CN)_6$ compounds were synthesized using iron nitrate nonahydrate, while Ru:$M'(CN)_6$ and Os:$M'(CN)_6$ involved the metal trichloride hydrate starting reagents. The dropwise addition was maintained at a constant rate by carefully pulling the plunger out of the filled syringe while secured to the flask by a septum and allowing gravity-driven dropping from the syringe needle. After 16 hours, the precipitated products were isolated by centrifugation at 8000 rpm. The obtained precipitates were resuspended in 40 mL water and centrifuged again for two more cycles, followed by 2 cycles of centrifugation/rinsing in 40 mL acetone and 2 rinsing cycles in 40 mL ethanol. To improve yield and prevent the product from remaining suspended in the reaction mixture after centrifugation, the compounds synthesized from potassium hexacyanoosmate were transferred to a dialysis membrane tubing (3000 Da MW cutoff) and purified for 4 cycles in a container of 2 liters deionized water at slow stirring.

Spectroscopy

UV-Vis-NIR absorption spectra of PBA films dropcast from aqueous suspension onto quartz slides were acquired using a JASCO V-770 spectrophotometer equipped with an integrating sphere. Raman spectra were acquired with an inVia Raman microscope (Renishaw) using a 633 nm laser at 0.1% power.

Powder X-ray diffraction

Powder X-ray diffraction measurements were performed on a PANalytical Empyrean diffractometer equipped with a PIXcel3D detector and operated at 44 kV and 40 kA using Cu Kα radiation (λ = 1.5406 Å).

DFT Calculations

First-principles plane-wave density functional theory (DFT) calculations were carried out using the Vienna *Ab initio* Simulation Package (VASP).[40] Electron-ion interactions were described by the projector-augmented-wave (PAW) method. The exchange-correlation interactions were first treated in the generalized gradient approximation (GGA) as parameterized in the Perdew-Burke-Ernzerhof (PBE) functional.[41] Because the PBE functional tends to underestimate the band gap and may give a wrong prediction of the magnetic ground state for PBAs, the screened Heyd–Scuseria–Ernzerhof hybrid functional (HSE06) was adopted for more accurate calculations.[17] For each PBA structure, we considered the primitive unit cell and introduced random small perturbations to the atomic positions using the VASPKIT program.[42] This allows DFT structural relaxations to locate distorted structures with lower symmetries that are more energetically stable.[10, 17] A Γ-centered 4×4×4 k-point sampling in the Brillouin zone was used with a plane-wave energy cutoff of 520 eV. Based on the HSE06 functional, both atomic positions and lattice constants were optimized until the residual forces were below 0.03 eV/Å. A ferromagnetic ordering between the two metal centers in the primitive unit cell was assumed. For PBAs, the carbon-coordinated metal ion assumes a low-spin (ls) electronic configuration, while the nitrogen-coordinated metal ion can be in a high-spin (hs) or ls electronic configuration.[17] Both the (hs, ls) and (ls, ls) configurations were considered in our calculations to determine which one is more stable. The spin-polarized atomic projected densities of state were processed using p4vasp.

ASSOCIATED CONTENT

Supporting Information

Supporting Information is available online.

Author Contributions

L. L. and D. A. R. designed and initiated the project. L. L. carried out theoretical calculations and data analysis. D. A. R. performed experiments and data analysis. N. W. contributed to materials synthesis and characterization. All the authors discussed the results and wrote the manuscript.

Acknowledgement

The theoretical calculations were supported by the Department of Energy (DOE) Office of Science Research Program for Microelectronics Codesign (sponsored by ASCR, BES, HEP, NP, and FES) through the Abisko Project. The synthesis and spectroscopic characterization (D. A. R. and A. A. T). were supported by the Reconfigurable Materials Inspired by Nonlinear Neuron Dynamics (REMIND) Energy Frontier Research Center, funded by the U.S. Department of Energy, Office of Science, Basic Energy Sciences, awarded to Texas A&M University (award #DE-SC0023353) and at Sandia National Laboratories under contract #DE-NA-0003525. This research used resources of the National Energy Research Scientific Computing Center (NERSC), a U.S. Department of Energy Office of Science User Facility operated under Contract No. DE-AC02-05CH11231. D. A. R. acknowledges Vitalie Stavila for x-ray diffraction training and resources.

Sandia National Laboratories is a multi-mission laboratory managed and operated by National Technology & Engineering Solutions of Sandia, LLC (NTESS), a wholly owned subsidiary of Honeywell International Inc., for the U.S. Department of Energy's National Nuclear Security Administration (DOE/NNSA) under contract DE-NA0003525. This written work is authored by an employee of NTESS. The employee, not NTESS, owns the right, title and interest in and to the written work and is responsible for its contents. Any subjective views or opinions that might be expressed in the written work do not necessarily represent the views of the U.S. Government. The publisher acknowledges that the U.S. Government retains a non-exclusive, paid-up, irrevocable, world-wide license to publish or reproduce the published form of this written work or allow others to do so, for U.S. Government purposes. The DOE will provide public access to results of federally sponsored research in accordance with the DOE Public Access Plan.

References

(1) Wang, L.; Lu, Y.; Liu, J.; Xu, M.; Cheng, J.; Zhang, D.; Goodenough, J. B. A Superior Low-Cost Cathode for a Na-Ion Battery. *Angewandte Chemie International Edition* **2013**, *52* (7), 1964-1967. DOI: https://doi.org/10.1002/anie.201206854.

(2) Kundu, D.; Talaie, E.; Duffort, V.; Nazar, L. F. The Emerging Chemistry of Sodium Ion Batteries for Electrochemical Energy Storage. *Angewandte Chemie International Edition* **2015**, *54* (11), 3431-3448. DOI: https://doi.org/10.1002/anie.201410376 (acccessed 2024/07/28).

(3) Song, J.; Wang, L.; Lu, Y.; Liu, J.; Guo, B.; Xiao, P.; Lee, J.-J.; Yang, X.-Q.; Henkelman, G.; Goodenough, J. B. Removal of Interstitial H2O in Hexacyanometallates for a Superior Cathode of a Sodium-Ion Battery. *Journal of the American Chemical Society* **2015**, *137* (7), 2658-2664. DOI: 10.1021/ja512383b.

(4) Wang, L.; Song, J.; Qiao, R.; Wray, L. A.; Hossain, M. A.; Chuang, Y.-D.; Yang, W.; Lu, Y.; Evans, D.; Lee, J.-J.; et al. Rhombohedral Prussian White as Cathode for Rechargeable Sodium-Ion Batteries. *Journal of the American Chemical Society* **2015**, *137* (7), 2548-2554. DOI: 10.1021/ja510347s.
(5) Qian, J.; Wu, C.; Cao, Y.; Ma, Z.; Huang, Y.; Ai, X.; Yang, H. Prussian Blue Cathode Materials for Sodium-Ion Batteries and Other Ion Batteries. *Advanced Energy Materials* **2018**, *8* (17), 1702619. DOI: https://doi.org/10.1002/aenm.201702619.
(6) Zhao, S.; Guo, Z.; Yan, K.; Guo, X.; Wan, S.; He, F.; Sun, B.; Wang, G. The Rise of Prussian Blue Analogs: Challenges and Opportunities for High-Performance Cathode Materials in Potassium-Ion Batteries. *Small Structures* **2021**, *2* (1), 2000054. DOI: https://doi.org/10.1002/sstr.202000054.
(7) Bhatt, P.; Kumar, A.; Yusuf, S. M. Multifunctional Properties and Potential Applications of Prussian Blue Analogue Magnets. *Chemistry of Materials* **2025**, *37* (2), 551-576. DOI: 10.1021/acs.chemmater.4c02904.
(8) Blasques, R. V.; Stefano, J. S.; Camargo, J. R.; Guterres e Silva, L. R.; Brazaca, L. C.; Janegitz, B. C. Disposable Prussian blue-anchored electrochemical sensor for enzymatic and non-enzymatic multi-analyte detection. *Sensors and Actuators Reports* **2022**, *4*, 100118. DOI: https://doi.org/10.1016/j.snr.2022.100118.
(9) Ying, S.; Chen, C.; Wang, J.; Lu, C.; Liu, T.; Kong, Y.; Yi, F.-Y. Synthesis and Applications of Prussian Blue and Its Analogues as Electrochemical Sensors. *ChemPlusChem* **2021**, *86* (12), 1608-1622. DOI: https://doi.org/10.1002/cplu.202100423 (acccessed 2025/03/09).
(10) Robinson, D. A.; Foster, M. E.; Bennett, C. H.; Bhandarkar, A.; Webster, E. R.; Celebi, A.; Celebi, N.; Fuller, E. J.; Stavila, V.; Spataru, C. D.; et al. Tunable Intervalence Charge Transfer in Ruthenium Prussian Blue Analog Enables Stable and Efficient Biocompatible Artificial Synapses. *Advanced Materials* **2023**, *35* (37), 2207595. DOI: https://doi.org/10.1002/adma.202207595.
(11) Sato, O.; Iyoda, T.; Fujishima, A.; Hashimoto, K. Photoinduced Magnetization of a Cobalt-Iron Cyanide. *Science* **1996**, *272* (5262), 704-705. DOI: doi:10.1126/science.272.5262.704.
(12) Sato, O.; Kawakami, T.; Kimura, M.; Hishiya, S.; Kubo, S.; Einaga, Y. Electric-Field-Induced Conductance Switching in FeCo Prussian Blue Analogues. *Journal of the American Chemical Society* **2004**, *126* (41), 13176-13177. DOI: 10.1021/ja046329s.
(13) Ferlay, S.; Mallah, T.; Ouahès, R.; Veillet, P.; Verdaguer, M. A room-temperature organometallic magnet based on Prussian blue. *Nature* **1995**, *378* (6558), 701-703. DOI: 10.1038/378701a0.
(14) Yu, Z.-Y.; Duan, Y.; Liu, J.-D.; Chen, Y.; Liu, X.-K.; Liu, W.; Ma, T.; Li, Y.; Zheng, X.-S.; Yao, T.; et al. Unconventional CN vacancies suppress iron-leaching in Prussian blue analogue pre-catalyst for boosted oxygen evolution catalysis. *Nature Communications*

2019, *10* (1), 2799. DOI: 10.1038/s41467-019-10698-9.
(15) Goberna-Ferrón, S.; Hernández, W. Y.; Rodríguez-García, B.; Galán-Mascarós, J. R. Light-Driven Water Oxidation with Metal Hexacyanometallate Heterogeneous Catalysts. *ACS Catalysis* **2014**, *4* (6), 1637-1641. DOI: 10.1021/cs500298e.
(16) Pintado, S.; Goberna-Ferrón, S.; Escudero-Adán, E. C.; Galán-Mascarós, J. R. Fast and Persistent Electrocatalytic Water Oxidation by Co–Fe Prussian Blue Coordination Polymers. *Journal of the American Chemical Society* **2013**, *135* (36), 13270-13273. DOI: 10.1021/ja406242y.
(17) Hurlbutt, K.; Giustino, F.; Pasta, M.; Volonakis, G. Electronic Structure and Electron-Transport Properties of Three Metal Hexacyanoferrates. *Chemistry of Materials* **2021**, *33* (17), 7067-7074. DOI: 10.1021/acs.chemmater.1c02183.
(18) Hegner, F. S.; Galán-Mascarós, J. R.; López, N. A Database of the Structural and Electronic Properties of Prussian Blue, Prussian White, and Berlin Green Compounds through Density Functional Theory. *Inorganic Chemistry* **2016**, *55* (24), 12851-12862. DOI: 10.1021/acs.inorgchem.6b02200.
(19) Ling, C.; Chen, J.; Mizuno, F. First-Principles Study of Alkali and Alkaline Earth Ion Intercalation in Iron Hexacyanoferrate: The Important Role of Ionic Radius. *The Journal of Physical Chemistry C* **2013**, *117* (41), 21158-21165. DOI: 10.1021/jp4078689.
(20) Yi, H.; Qin, R.; Ding, S.; Wang, Y.; Li, S.; Zhao, Q.; Pan, F. Structure and Properties of Prussian Blue Analogues in Energy Storage and Conversion Applications. *Advanced Functional Materials* **2021**, *31* (6), 2006970. DOI: https://doi.org/10.1002/adfm.202006970.
(21) Cattermull, J.; Sada, K.; Hurlbutt, K.; Cassidy, S. J.; Pasta, M.; Goodwin, A. L. Uncovering the Interplay of Competing Distortions in the Prussian Blue Analogue K2Cu[Fe(CN)6]. *Chemistry of Materials* **2022**, *34* (11), 5000-5008. DOI: 10.1021/acs.chemmater.2c00288.
(22) Hurlbutt, K.; Giustino, F.; Volonakis, G.; Pasta, M. Origin of the High Specific Capacity in Sodium Manganese Hexacyanomanganate. *Chemistry of Materials* **2022**, *34* (10), 4336-4343. DOI: 10.1021/acs.chemmater.1c04167.
(23) Wojdeł, J. C.; de P. R. Moreira, I.; Bromley, S. T.; Illas, F. On the prediction of the crystal and electronic structure of mixed-valence materials by periodic density functional calculations: The case of Prussian Blue. *The Journal of Chemical Physics* **2008**, *128* (4). DOI: 10.1063/1.2824966 (acccessed 7/15/2024).
(24) Wojdeł, J. C. First principles calculations on the influence of water-filled cavities on the electronic structure of Prussian Blue. *Journal of Molecular Modeling* **2009**, *15* (6), 567-572. DOI: 10.1007/s00894-008-0425-6.
(25) Wojdeł, J. C.; Moreira, I. d. P. R.; Bromley, S. T.; Illas, F. Prediction of half-metallic conductivity in Prussian Blue derivatives. *Journal of Materials Chemistry* **2009**, *19*

(14), 2032-2036, 10.1039/B813788A. DOI: 10.1039/B813788A.
(26) Becke, A. D. Density‐functional thermochemistry. III. The role of exact exchange. *The Journal of Chemical Physics* **1993**, *98* (7), 5648-5652. DOI: 10.1063/1.464913 (acccessed 7/29/2024).
(27) Robin, M. B. The Color and Electronic Configurations of Prussian Blue. *Inorganic Chemistry* **1962**, *1* (2), 337-342. DOI: 10.1021/ic50002a028.
(28) Behera, J. N.; D'Alessandro, D. M.; Soheilnia, N.; Long, J. R. Synthesis and Characterization of Ruthenium and Iron−Ruthenium Prussian Blue Analogues. *Chemistry of Materials* **2009**, *21* (9), 1922-1926. DOI: 10.1021/cm900230p.
(29) Keggin, J. F.; Miles, F. D. Structures and Formulæ of the Prussian Blues and Related Compounds. *Nature* **1936**, *137* (3466), 577-578. DOI: 10.1038/137577a0.
(30) Buser, H. J.; Schwarzenbach, D.; Petter, W.; Ludi, A. The crystal structure of Prussian Blue: Fe4[Fe(CN)6]3.xH2O. *Inorganic Chemistry* **1977**, *16* (11), 2704-2710. DOI: 10.1021/ic50177a008.
(31) Solovyev, I. V.; Dederichs, P. H.; Anisimov, V. I. Corrected atomic limit in the local-density approximation and the electronic structure of d impurities in Rb. *Physical Review B* **1994**, *50* (23), 16861-16871. DOI: 10.1103/PhysRevB.50.16861.
(32) Feng, Q.; Ekholm, M.; Tasnádi, F.; Jönsson, H. J. M.; Abrikosov, I. A. Topological transitions of the Fermi surface of osmium under pressure: an LDA+DMFT study. *New Journal of Physics* **2017**, *19* (3), 033020. DOI: 10.1088/1367-2630/aa5f8e.
(33) Kesavan, J. K.; Fiore Mosca, D.; Sanna, S.; Borgatti, F.; Schuck, G.; Tran, P. M.; Woodward, P. M.; Mitrović, V. F.; Franchini, C.; Boscherini, F. Doping Evolution of the Local Electronic and Structural Properties of the Double Perovskite Ba2Na1−xCaxOsO6. *The Journal of Physical Chemistry C* **2020**, *124* (30), 16577-16585. DOI: 10.1021/acs.jpcc.0c04807.
(34) Liu, X.-L.; Li, Y.; Xu, Q.-D.; Yang, Y.-Y.; Fu, J.-H.; Wu, X.-T.; Sheng, T.-L. Influence of the CN Orientation on the Degree of Electron Delocalization of Ru−Ru−Ru Mixed-Valent Complexes. *Inorganic Chemistry* **2022**, *61* (44), 17392-17401. DOI: 10.1021/acs.inorgchem.2c01172.
(35) Siddiqui, S.; Henderson, W. W.; Shepherd, R. E. Pentacyanoruthenate(II)-pentaammineruthenium(II/III) binuclear complexes bridged by cyanogen, cyanide, and 4,4'-bipyridine. *Inorganic Chemistry* **1987**, *26* (19), 3101-3107. DOI: 10.1021/ic00266a009.
(36) Pieslinger, G. E.; Alborés, P.; Slep, L. D.; Baraldo, L. M. Class III Delocalization in a Cyanide-Bridged Trimetallic Mixed-Valence Complex. *Angewandte Chemie International Edition* **2014**, *53* (5), 1293-1296. DOI: https://doi.org/10.1002/anie.201307025 (acccessed 2025/02/11).
(37) Neff, V. D. Electrochemical Oxidation and Reduction of Thin Films of Prussian Blue. *J. Electrochem. Soc.* **1978**, *125* (6), 886-887. DOI: 10.1149/1.2131575. Xidis, A.;

Neff, V. D. On the Electronic Conduction in Dry Thin Films of Prussian Blue, Prussian Yellow, and Everitt's Salt. *J. Electrochem. Soc.* **1991**, *138* (12), 3637-3642. DOI: 10.1149/1.2085472.
(38) Talin, A. A.; Meyer, J.; Li, J.; Huang, M.; Schwacke, M.; Chung, H. W.; Xu, L.; Fuller, E. J.; Li, Y.; Yildiz, B. Electrochemical Random-Access Memory: Progress, Perspectives, and Opportunities. *Chem. Rev.* **2025**, *125* (4), 1962-2008. DOI: 10.1021/acs.chemrev.4c00512.
(39) Curtis, J. C.; Meyer, T. J. Outer-sphere charge transfer in mixed-metal ion pairs. *Inorg. Chem.* **1982**, *21* (4), 1562-1571. DOI: 10.1021/ic00134a059.
(40) Kresse, G.; Furthmüller, J. Efficiency of ab-initio total energy calculations for metals and semiconductors using a plane-wave basis set. *Computational Materials Science* **1996**, *6* (1), 15-50. DOI: https://doi.org/10.1016/0927-0256(96)00008-0.
(41) Perdew, J. P.; Burke, K.; Ernzerhof, M. Generalized Gradient Approximation Made Simple. *Physical Review Letters* **1996**, *77* (18), 3865-3868. DOI: 10.1103/PhysRevLett.77.3865.
(42) Wang, V.; Xu, N.; Liu, J.-C.; Tang, G.; Geng, W.-T. VASPKIT: A user-friendly interface facilitating high-throughput computing and analysis using VASP code. *Computer Physics Communications* **2021**, *267*, 108033. DOI: https://doi.org/10.1016/j.cpc.2021.108033.

Supporting Information

Understanding and Tuning the Electronic Properties of Prussian Blue Analogues

Liangbo Liang[+*], Donald A. Robinson[‡*], Nova Wu[‡,ɬ], Michael E. Foster[‡], Petro Maksymovych[+], A. Alec Talin[‡], Bobby G. Sumpter[+]

[+]*Center for Nanophase Materials Sciences, Oak Ridge National Laboratory, Oak Ridge, Tennessee 37831, United States*

[‡]*Sandia National Laboratories, Livermore, CA 94550, United States*

[ɬ]*Stanford University, Stanford, CA 94305, United States*

[*]Corresponding authors: liangl1@ornl.gov; darobin@sandia.gov.

Contents

1. UV/Vis/NIR spectra deconvolution

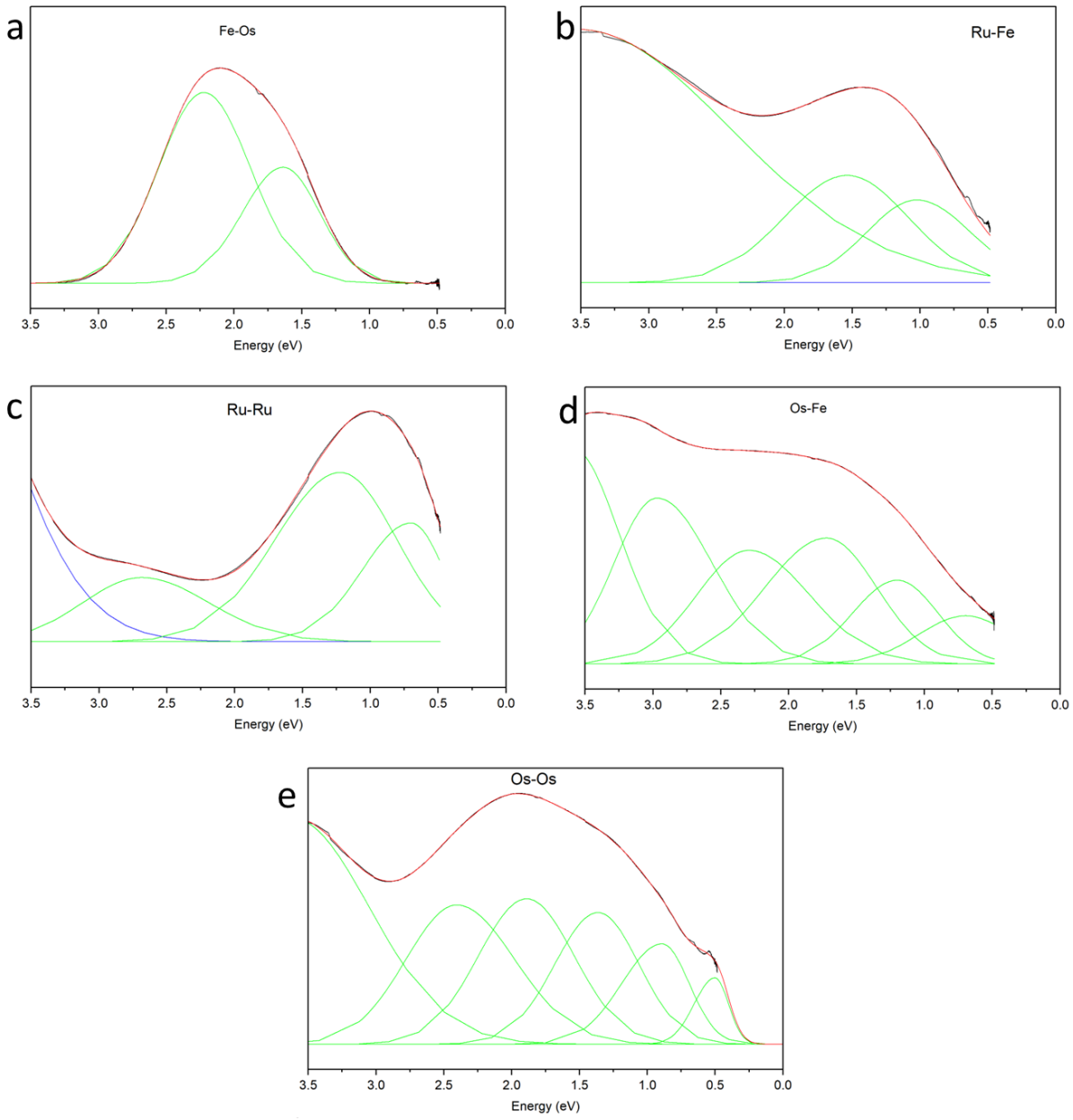

Figure S3. Deconvolution of UV/Vis/NIR spectra for PBAs that exhibited evidence of multiple IVCT transitions.

2. Powder X-ray diffraction

Sharper diffraction peaks are observed for Fe_N-M_C PBAs in comparison to Ru_N-M_C and Os_N-M_C compounds, indicating poorer crystallinity for the latter materials. The peak positions for the Ru_N and Os_N compounds roughly align with the expected face-centered cubic symmetry of the PBA structure, but the extreme broadness of the diffraction lines suggests very short-range order and an essentially amorphous structure.

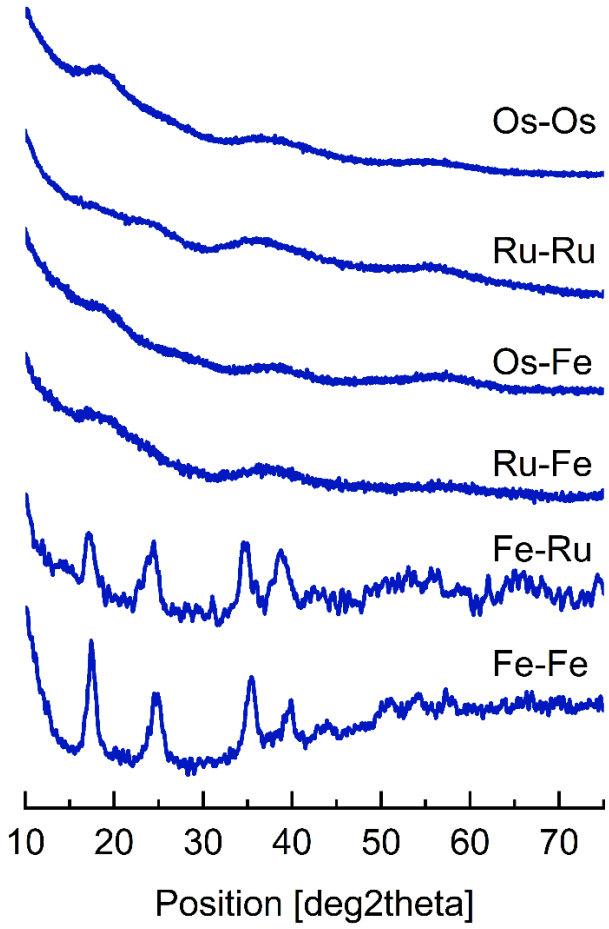

Figure S4. Powder X-ray diffraction (XRD) patterns for M_N-M_C Prussian blue analogs.